Improved design of micromachined lateral suspensions using intermediate frames

2007 J. Micromech. Microeng. 17 1680

(http://iopscience.iop.org/0960-1317/17/8/035)

J. Micromech. Microeng. **17** (2007) 1680–1694 doi:10.1088/0960-1317/17/8/035

Improved design of micromachined lateral suspensions using intermediate frames

W T Pike and S Kumar

Optical and Semiconductor Devices Group, Department of Electrical and Electronic Engineering, Imperial College, London SW7 2AZ, UK

E-mail: w.t.pike@imperial.ac.uk

Received 2 March 2007, in final form 15 May 2007
Published 20 July 2007
Online at stacks.iop.org/JMM/17/1680

Abstract
A complete analysis of the translational and rotational modes of a model lateral suspension is presented. The derived formulae quantify spurious-mode resonant frequencies for cross-axis translation and rotation, and on-axis translation, and can provide very simple expressions for the rejection ratios in terms of the geometry of the suspensions. It is shown that the introduction of intermediate frames, coupling equivalent points of the lateral suspension either side of the suspended mass, can provide much improved dynamics. To investigate the derived relationships, suspensions have been fabricated using through-wafer deep reactive-ion etching (DRIE). Using analysis of the suspension dynamics under the rastered beam of a scanning electron microscope, the various modes of the suspension have been visualized and quantified. These observations are in good agreement with the derived formulae, taking into account the actual profile of the beams fabricated in DRIE. Further finite element analysis across a broad range of suspensions is consistent with the derived formulae. A design heuristic is provided for rapidly optimizing micromachined lateral suspensions by incorporating intermediate frames.

1. Introduction

For many mechanical systems, both sensors and actuators, it is important to confine the motion of the prime moving part to one direction. Flexures are very often used to produce smooth and controllable motion with minimum hysteresis. In microelectromechanical systems (MEMS), with their adverse scaling of frictional forces with reduced mechanism size, flexures are most often the kinematic link of choice. However, flexures provide imperfect guided motion: unwanted modes will always be present in off-axis degrees of freedom and performance in the compliant direction is limited by additional modes with frequencies above the fundamental. This work establishes a design approach for lateral suspensions machined in silicon wafers, with particular reference to the high-aspect ratios achievable using deep reactive-ion etching.

Lateral suspensions have been often utilized in MEMS to produce resonant structures, from early surface-micromachined comb-driven resonators [1, 2], through commercial devices such as the analog devices accelerometer series [3, 4] and more recently in deep reactive-ion-etched (DRIE) accelerometers [5–7], polymer accelerometers [8, 9] and gyroscopes [10]. Optical devices employ DRIE lateral suspensions for alignment, both rotational [11] and translational [12].

In all these devices performance will be enhanced by maximizing the separation of the fundamental and other unwanted modes, giving a maximum clean bandwidth for the suspension [13, 14]. The behavior of the fundamental mode of lateral suspensions can be analyzed in terms of a one-degree-of-freedom (1DOF) system [1, 2], which neglects all potential spurious modes. Finite element analysis (FEA), which is able to extract any number of spurious modes, has been applied to the uniaxial suspension of the analog devices accelerometer [15]. Analytic approaches and FEA have been used to optimize the design of a dual-axis suspension [16].

In this work a canonical folded-cantilever lateral suspension of the simplest symmetric design is first

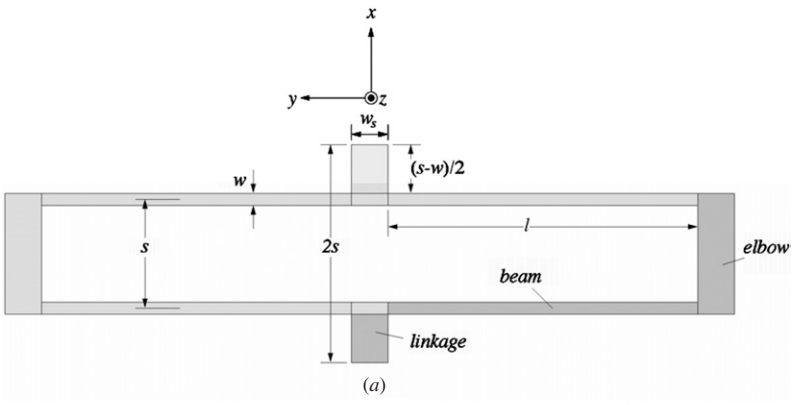

(*a*)

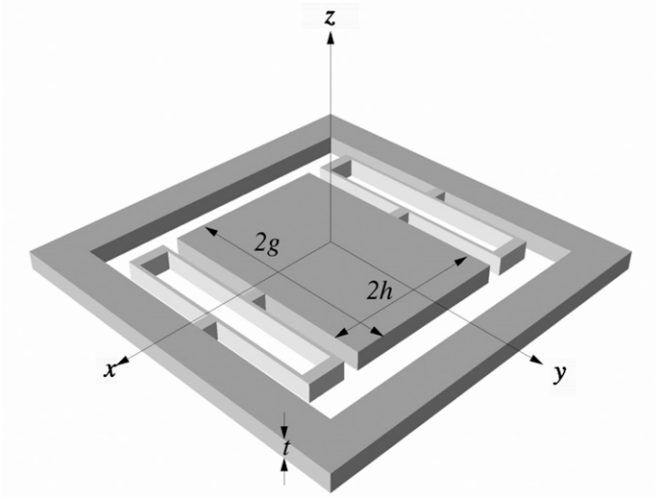

(*b*)

Figure 1. Schematic of lateral suspension showing (*a*) a single suspension unit illustrating the model geometry and critical dimensions and (*b*) the overall geometry of the suspension.

considered. A complete set of analytic expressions is derived for the six degrees of freedom (6 DOF). Further modes due to the finite mass of the suspension are then included. Under some rather non-restrictive assumptions it is shown that the spurious-mode rejection ratios can be well estimated using simple multiples of the aspect ratios of the suspensions. Next, additional suspension units are included to lower the fundamental frequency and the introduction of intermediate frames coupling portions of this suspension is explored as a novel approach for enhancing the performance. A full set of analytical equations is presented for the off-axis modes of a suspension incorporating such frames. This analysis is applied to a suspension fabricated for low-frequency excitation. The effects of non-ideal fabrication of the structures due to overetching of the sidewalls of the suspension are quantified. Hence the introduction of intermediate frames is demonstrated and quantified as path to improve the performance of lateral suspensions.

2. Design

2.1. Lateral suspensions

The lateral suspension is shown schematically in figure 1. Geometrically, the suspension is an extrusion of a two-dimensional pattern. Physically, the depth of the extrusion is given by the thickness of the etched layer, which in this work is the full wafer thickness. The suspension consists of two springs either side of a platform/proof mass connected to an external fixed frame. The ideal suspension would be solely compliant along the x-axis with maximum stiffness to translations along the other two axes and rigidity to rotation about all axes, that is to roll about the x-axis, pitch about the y-axis and yaw about the z-axis. It is assumed that the suspended mass is perfectly rigid, justifiable if the second moment of area of the proof mass along any axis is much greater than the smallest second moment of area of a suspension element. It is further assumed, at least initially, that the suspension is massless, which is reasonable when considering cross-axis dynamics. A massive suspension will be later treated as a perturbation on the massless solution. Under these assumptions the analysis of such a suspension involves the solution of the equations of motion for a 6DOF system [17]:

$$\mathbf{M\ddot{u}} + \mathbf{C\dot{u}} + \mathbf{Ku} = \mathbf{0} \tag{1}$$

where $\mathbf{u}$ is the coordinate vector, $\mathbf{u} = [x, y, z, \theta_x, \theta_y, \theta_z]^T$, $\mathbf{M}$ is the inertial matrix which, as well as the diagonal components $(m, m, m, I_{xx}, I_{yy}, I_{zz})$, where m is the suspended mass and I_{ij} are the moments of inertia, will in general have symmetric off-diagonal products of inertia I_{jk}, $\mathbf{C}$ is a symmetric matrix of the damping terms and $\mathbf{K}$ is a symmetric stiffness matrix. The six

simultaneous equations for the general case become separable in their coordinates if there are three planes of symmetry to the suspension [18]. Such a suspension of point group *mmm* has no coupling between motion in each coordinate—all the off-diagonal terms in **M** and **C** are zero. This decoupling not only greatly simplifies analysis but is necessary if the suspension is used for transduction. Hence, this work considers only such center-of-gravity systems, so called as symmetry implies that the elastic forces of the suspension are directed through the center of the suspended mass. In addition, the system is further simplified by neglecting damping as the aim of this work is to optimize the design in terms of compliance. The resulting six separable equations are

$$[m \quad m \quad m \quad I_{xx} \quad I_{yy} \quad I_{zz}] \begin{bmatrix} \ddot{x} \\ \ddot{y} \\ \ddot{z} \\ \ddot{\alpha} \\ \ddot{\beta} \\ \ddot{\gamma} \end{bmatrix} - [k_x \quad k_y \quad k_z \quad k_\alpha \quad k_\beta \quad k_\gamma] \begin{bmatrix} x \\ y \\ z \\ \alpha \\ \beta \\ \gamma \end{bmatrix} = 0, \tag{2}$$

which have the customary normal-mode solution, $u_i = a_i \sin(\omega t + \phi)$ where normal-mode frequencies of

$$\omega_i = \sqrt{K_{ii}/M_{ii}} \tag{3}$$

with a_i and ϕ are set by the initial conditions. The spring constants, and hence the frequencies of the normal modes, determine the performance of the suspension. To optimize, the frequency ratio of the cross-axis modes to the on-axis mode, $\omega_{i\neq x}/\omega_x$, should all be as high as possible. As there are often opposing effects on the various rejection ratios $\omega_{i\neq x}/\omega_x$ for a particular design parameter, an optimum suspension design will in general have its two lowest cross-axis-mode frequencies approximately equal.

In addition to the symmetry, there are further constraints on the design of the suspension. It should be manufacturable in DRIE (i.e., formed by the projection of a two-dimensional structure, with some requirements on minimum feature size and separation). A minimal area (and hence cost) should be required for fabrication. The suspension should give sufficient throw for any required motion in the compliant direction. Suspension beam spacings should be chosen to control squeeze-film damping (often required to be either critical or minimized). The general design solution is a suspension that is sinuous, maximizing its length perpendicular to the compliant direction, while maintaining rigidity to cross-axis forces by minimizing its overall size along the compliant direction.

2.2. On-axis compliance

Folded cantilever beams have been a frequent design choice to best accommodate these constraints in lateral suspensions [9, 12, 19–23]. A cantilever has a spring constant dependent on I, the bending constant in the compliant direction which is given by the second moment of area of the beam. The beam profile achieved by DRIE can be different from the model rectangular geometry [24–27] and so I is best maintained as the cross-sectional parameter in the analysis. A folded cantilever consisting of beams with length l and Young's modulus E has a spring constant of $6EI/l^3$ if the 'elbow' at the fold is taken to be rigid to torques about the z-direction. This assumption is valid for most reasonable elbow geometries.

A series of n folded cantilevers each of spring constant k will have a summed spring constant of k/n. As well as softening the suspension, the use of multiple units improves the linearity as the deflection of each cantilever is a lower multiple of the beam thickness. However, a simple series of folded cantilevers lacks symmetry in the plane perpendicular to both the compliant and cantilever direction and to avoid the dynamic and analytical problems of cross-coupling between the axes mentioned earlier, the unit of suspension is taken as a mirror pair of folded cantilevers, which reintroduces the plane of symmetry to the resulting center-of-gravity system. The cantilever pairs are linked at their central attachment points as shown in the schematic of figure 1(*a*). This results in increased stiffness to rotation about the z-axis compared to an unconnected pair for multiple suspension units. The planar geometry of each unit can be characterized by the values of the beam length l, beam width w, beam spacing (taken beam axis to beam axis) s, linkage length width w_s, and linkage length, taken here to be $(s-w)/2$ to give a unit dimension in the compliant direction of $2s$. The detailed elbow geometry is left undefined. There are two important geometric ratios defining the suspension; the beam cross-sectional aspect ratio, w/t; the suspension ratio of the beam spacing to the beam length, s/l. The simplest suspension consists of one unit on each side of the proof mass (figure 1(*b*)). Such a suspension satisfies the required symmetry conditions and the six spring constants can be solved separately for motion along and about each axis.

The canonical status of this suspension is evident in its application in a number of designs, e.g. [28–32]. A detailed analysis of this suspension is therefore justified in order to set a rational design methodology. One obvious approach, optimization through FEA, has already been applied to this suspension design in order to optimize a particular feature of its application [15] but FEA does not produce general design rules. The analytical formulae provided in this work should provide a more heuristic approach to lateral suspension design. In deriving these analytical formulae, FEA (ANSYS, Inc., Canonsburg, PA) was applied to elements of the suspension to ensure that all the important modes of deflections were included, and also to crosscheck numerically the analytical expressions. In order to produce reasonable FEA simulation run times and node numbers the suspension was taken as a simple extrusion, with an effective beam width to try to take into account the effects of the etch profile. The extrusion was performed on an initial 2D meshing to produce monoclinic elements, rather than triclinic elements, and the mode shapes and frequencies were calculated using the ANSYS implementation of the block Lanczos method.

In the first instance, the minimal suspension consisting of a single suspension unit either side of the proof mass is considered. In the compliant direction the spring constant of the total suspension will be given by

$$k_x = \frac{24EI_x}{nl^3}. \tag{4}$$

To maximize the compliance along this direction for a suspension fabricated in an anisostropic crystal such as silicon, the beams should be orientated to minimize E. For silicon this corresponds to the $\langle 1\,0\,0\rangle$ directions [33].

2.3. Cross-axis translational compliance

Cross-axis translational compliance of the complete suspension is determined by the spring constants in the y and z directions, which in turn are derived by considering the deflections of the suspended mass due to a test force applied at the centroid of the mass in the required direction.

The deflection in the out-of-plane z direction, often the most important deflection to minimize, is considered first. The linkages are assumed perfectly rigid. If a force F_z is impressed in the z direction at the centroid of the proof mass, this will result in a force $F_z/4$ on the end face of the beam nearest the proof mass. Balancing forces and torques for each beam implies that all the vertical forces are $F_z/4$, the twisting torques are given by $T = F_z s/8$, and the end torques are $F_z l/4$. The total deflection in the z direction is the sum of the deflection at the elbow, Δ_{elbow}, as a result of the twisting of the beams from the torque T and the two cantilever deflections, Δ_{beam}, of the beams as a result of the impressed forces and torques.

This torque will produce a constant twist along each beam [19], and produce a resulting deflection at the elbows given by

$$\Delta_{\text{elbow}} = \frac{F_z l s^2}{8GJ} \tag{5}$$

for small loads where G is the relevant shear modulus for the beam direction, and J is the torsion constant, which depends only on the cross-sectional dimensions of the beam. The beam deflection will be given by $F_z l^3/(48EI_z)$ where the elbow is considered as completely rigid. The rigidity of the elbow about this axis is much more difficult to maintain compared to the rigidity about the z-axis for deflections in the compliant x direction. If the elbow has no rigidity each beam acts as a single cantilever with a maximum angle of deflection at the elbow and the beam deflection is $F_z l^3/(12EI_z)$. Hence an elbow-compliance factor, c, which depends on the rigidity of the elbow and varies between a value of 1 and 4, is introduced into the analysis:

$$\Delta_{\text{beam}} = \frac{cFl^3}{48EI_z}\,. \tag{6}$$

Figure 2 shows this compliance factor for some representative geometries as determined by FEA. Where present the elbow cross bar is half the beam spacing s from the end on the elbow. It is evident that to minimize the z-axis deflection some webbing of the elbow is required. A semicircular elbow geometry with a cross bar, unfilled, represents a reasonable compromise between good stiffness and low suspension mass.

The spring constant for deflections in the z direction is given by

$$\frac{1}{k_z} = \frac{ls^2}{8GJ} + \frac{cl^3}{24EI_z}. \tag{7}$$

The inverse square of the rejection ratio for the z mode is therefore

$$\frac{k_x}{k_z} = 3\frac{EI_x s^2}{GJl^2} + \frac{cI_x}{I_z}. \tag{8}$$

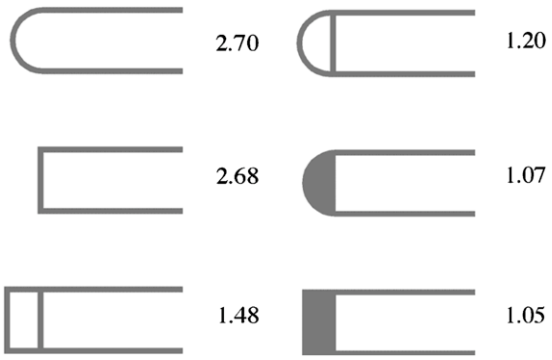

Figure 2. The values of the compliance from FEA are shown for a variety of representative elbow geometries, with 4 corresponding to completely compliant, and 1 completely rigid. A beam aspect ratio of 1:20 was simulated.

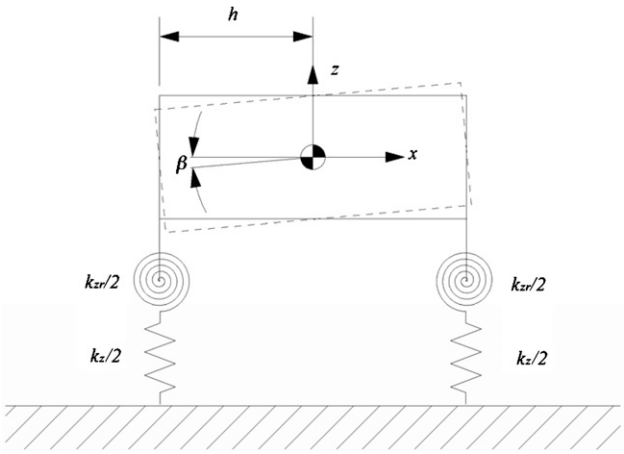

Figure 3. Schematic showing decomposition of the rotational compliance into translational and rotational components.

Considering the y-axis compliance of the suspension, a compressive axial force F equal to $F_y/4$ is applied to the face of the beam nearest the proof mass. The end torque to the beams will be $T = Fs/2$. The end-deflection angle of each beam, and hence the rotation of the elbow, θ, produces a deflection of the proof mass of $s\theta$, giving a spring constant in the y direction of

$$k_y = \frac{8EI_x}{ls^2}. \tag{9}$$

The rejection of the y mode is therefore given by $l/(\sqrt{3}s)$.

2.4. Rotational compliance

The rotational spring constants about the y and z axes, k_β and k_γ, can be decomposed into contributions from the effective translational springs with additional torques due to the effective torsional springs. Figure 3 shows the geometry for the y-axis, where h is half the length of the suspended mass. For this geometry, for a torsional spring constant of k_{zr}, the rotational spring constant will be given by

$$\begin{aligned} k_\beta &= k_z h^2 + k_{zr} \\ &\geqslant k_z h^2 \end{aligned} \tag{10}$$

The corresponding frequency ω_β of rotation of the suspended mass about the y-axis is given from [3] by

$$\omega_\beta = \sqrt{\frac{k_\beta}{I_{yy}}}. \tag{11}$$

Neglecting for the moment the torsional contribution of the suspension, this gives for $I_{yy} = {}^1/_3 mh^2$ (as $h \gg t$)

$$\omega_\beta = \sqrt{\frac{3k_z}{m}}. \tag{12}$$

Hence the ratio of the frequency of the rotational mode about the y-axis to the translational mode about the z-axis is

$$\frac{\omega_\beta}{\omega_z} = \sqrt{3}. \tag{13}$$

Similarly for rotation about the z-axis, again neglecting torsional effects,

$$\omega_\gamma = \sqrt{\frac{3k_y}{m(1+g^2/h^2)}} \qquad \text{and} \qquad \frac{\omega_\gamma}{\omega_y} = \frac{\sqrt{3}}{\sqrt{1+g^2/h^2}}, \tag{14}$$

where g is the half width of the proof mass. Therefore maximizing the off-axis translational-mode frequencies will automatically maximize the off-axis rotational-mode frequencies, simplifying the design approach.

Considering (10), the additional torsional contribution will cause the rotational-mode frequencies to be increased. Summing appropriately the torsion of all the beams, the equivalent spiral spring will have an angular spring constant of

$$k_{zr} = \frac{GJ}{2l}. \tag{15}$$

For a large-aspect-ratio beam geometry, (23) will give

$$k_\beta = \frac{8GJ}{2ls^2}\left(1 + \frac{s^2}{16h^2}\right) \tag{16}$$

and as $s \ll h$, the second, torsional term can be neglected.

The rotational mode about the x-axis requires separate consideration. The angular deflection consists of a contribution from the twisting of the linkages about their x-axes and a more complex contribution from a combination of twisting and bending of the beams. Taking the twisting of the linkages first, as there are two linkages for each spring unit of the suspensions on each side of the suspended mass, each of length $(s-w)/2$, the torsional spring constant $k_{\alpha,\text{link}}$ will be

$$k_{\alpha,\text{link}} = \frac{2GJ_s}{s-w}, \tag{17}$$

where J_s is the torsion constant of the linkage. The torsional compliance of the linkages can be made very low by increasing the width of the linkage. The compliance due to the distortion of the beams will then dominate. For a total external torque of τ, each beam will experience a torque $T = \tau/4$ on its connecting face to the linkage to the proof mass. This torque will be opposed by a combination of a torque U and moment Fl provided by the elbow. The external torque can therefore be regarded as being distributed between the bending torque U and force F so that the resulting deflection and twist of the beams cause a pure pivot of the suspension unit about this center axis. The resulting torsional spring constant due to the distortion of the beams for a single suspension unit each side of the suspended mass, $k_{\alpha,\text{beam}}$, can be solved as

$$\frac{1}{k_{\alpha,\text{beam}}} = \frac{1}{4EI_z}\left(1 - \frac{3}{4 + 3\frac{EI_z s^2}{GJl^2}}\right). \tag{18}$$

The total compliance will be the sum of the compliances due to the torsion of the linkages derived from (17) and (24):

$$\frac{1}{k_\alpha} = \frac{1}{k_{\alpha,\text{link}}} + \frac{1}{k_{\alpha,\text{beam}}}. \tag{19}$$

The linkage width should therefore be chosen to restrict the contribution of the torsion of the linkage to the total compliance. The condition $k_{\alpha,\text{link}} \gg \max\ k_{\alpha,\text{beam}}$ for a comparatively stiff linkage corresponds, for $s \gg w$, to

$$w_s \gg \left[2\frac{E}{G}\left(\frac{t}{w}\right)^2 \frac{s}{l}\right]^{1/3} w. \tag{20}$$

As the beam aspect ratio and suspension aspect ratio will often be comparable, and certainly no more than fifty each, condition (20) will be met for a linkage of width, w_s, greater than about ten times the beam width, w.

For a moment of inertia about the x-axis of

$$I_{xx} = \tfrac{1}{3} m g^2 \tag{21}$$

the square of the rejection ratio for this mode will be given by

$$\left(\frac{\omega_\alpha}{\omega_x}\right)^2 = \left\{\frac{4EI_x(s-w)g^2}{GJ_s l^3} + \frac{4I_x g^2}{I_z l^2}\left[1 - \frac{3}{4 + \frac{3s^2 EI_z}{l^2 GJ}}\right]\right\}^{-1}. \tag{22}$$

The analytical expressions for all six modes are shown in table 1.

2.5. *Effect of suspension mass*

Up to this point the suspension has been considered as massless. However, the mass of the beams will both reduce the frequency of the fundamental and produce additional modes in all degrees of freedom. The frequency will be reduced according to Rayleigh's method [17], to

$$\omega_x = \sqrt{\frac{k_x}{m + \frac{33}{140}m_s}}, \tag{23}$$

where m_s is the total mass of the suspension. For most suspension designs, $m \gg m_s$, and the mass-loading effect is very small. Corresponding reductions will be seen for the other modes. If the suspension mass is comparable to the suspended mass, m in table 1 should be replaced by $m + \frac{33}{140}m_s$.

The most important additional modes are in the x direction, as they will be excited by the same signals as the fundamental. In general, an analytical solution is not obtainable. One can split the suspension into a series of discrete masses separated by massless springs. Unless the number of elements is low, the resulting analysis gives little physical insight. Alternatively the suspension can be considered as having both a continuously distributed mass and spring constant. This approach gives simpler results, more amenable to design optimization. Treating the spring as a uniformly distributed mass is self-consistent if the resulting modes have periodicities that are much greater than the

Table 1. Expressions for the fundamental and lowest spurious modes for a lateral suspension with single suspension unit either side of the proof mass for the general case, rectangular beam cross sections, and assuming equal beam and suspension aspect ratios.

Mode, i	ω_i^2	$\frac{\omega_x^2}{\omega_i^2}$ for rectangular beam cross sections, $E/G = 3$, and rigid, width less links and elbows, and square proof mass	$\frac{\omega_x^2}{\omega_i^2}$, with $s/l = w/t = R$
x	$\frac{24EI_x}{ml^3}$	1	1
x_1	$\pi^2 \frac{m}{m_s}\omega_x^2$	$\frac{2}{\pi^2}\frac{w}{h}$	$\frac{2}{\pi^2}\frac{t}{h}R$
y	$\frac{8EI_x}{mls^2} = \frac{l^2}{3s^2}\omega_x^2$	$3\frac{s^2}{l^2}$	$3R^2$
z	$\frac{1}{\frac{mls^2}{8GJ}+\frac{mcl^3}{24EI_z}} = \frac{\omega_x^2}{\frac{3EI_x s^2}{GJl^2}+\frac{cI_x}{I_z}}$	$\frac{s^2}{l^2}+\frac{w^2}{t^2}$	$2R^2$
α	$\left\{\frac{4EI_x(s-w)g^2}{GJ_s l^3}+\frac{4I_x g^2}{I_z l^2}\left[1-\frac{3}{4+\frac{3s^2EI_z}{l^2GJ}}\right]\right\}^{-1}\omega_x^2$	$4\frac{w^2}{t^2}\left(1-\frac{3}{4+\frac{1}{4}\frac{s^2}{l^2}\frac{t^2}{w^2}}\right)$	$\sim R^2$
β	$3\omega_z^2$	$\frac{1}{3}\left(\frac{s^2}{l^2}+\frac{w^2}{t^2}\right)$	$\frac{2}{3}R^2$
γ	$\frac{3}{1+g^2/h^2}\omega_y^2$	$2\frac{s^2}{l^2}$	$2R^2$

periodicities in the distribution of the mass of the spring along the compliant direction. For the suspension geometry under consideration this implies that the mode periods should be much greater than s, the spring spacing.

Consideration of the mass of the suspension introduces additional on-axis modes with the displacement in the x direction of the suspensions on either side either symmetric or antisymmetric about the suspended mass [34]. The symmetric mode has a node at the suspended mass and is therefore relatively benign to the overall dynamic performance. However, the antisymmetric mode drives an oscillation of the suspended mass, the amplitude of which is proportional to m_s/m. The ratio of the frequencies of the first harmonic ω_{x1} to the fundamental to first order in m_s/m for both modes is

$$\frac{\omega_{x1}}{\omega_x} \approx \pi\sqrt{\frac{m}{m_s}}. \tag{24}$$

In summary, consideration of the mass of the springs reveals a small reduction in the fundamental frequency (which can normally be neglected) and additional on-axis normal modes, both symmetric and antisymmetric about the suspended mass. The lowest frequency antisymmetric mode is of particular concern as motion of the suspended mass will occur. Both the amplitude and frequency of this mode depend on the ratio m/m_s, linearly and to the square root respectively, and hence it is important to minimize the mass of the springs as far as possible.

2.6. Estimators for the rejection ratios of the spurious modes

By making some reasonable approximations, it is possible to achieve some very simple expressions for the rejection ratios of all the spurious modes. First, the beam cross sections are assumed to be rectangular. Second, the ratio of Young's modulus to the shear modulus, E/G, is assumed to be 3, which corresponds to an incompressible solid (for silicon [1 0 0] E/G is 2.56 [33]). Third, it is assumed that the linkages and elbows are completely rigid ($c = 1$ and $1/k_{\alpha,\,\mathrm{link}} = 0$) and of zero width. In this case the suspension mass will be $8lw$. Fifth, the suspension is assumed to extend the width of the proof mass so that $l = g$. Last, the proof mass is assumed to be square. Under these conditions, the rejection ratios are shown in the final column of table 1. Further, if it is assumed that the suspension and beam aspect ratios are equal, $s/l = w/t = R$, the simple multiples shown in the final column are obtained.

2.7. Introduction of frames for multiple suspension units

It is very often desirable to reduce the fundamental frequency of a lateral suspension as far as possible. For instance, below the fundamental frequency, the displacement of the proof mass due to an applied acceleration is inversely proportional to the square of the fundamental frequency, and so to maximize the sensitivity, if used in an accelerometer, the fundamental frequency of the lateral suspension should be minimized. For a given device area this can be achieved by either reducing the width of the beams or adding additional suspension units on either side of the proof mass. There is a limit to how thin the beams can be fabricated due to inherent process limitations and so the addition of suspension units may be required. The spring constant for the fundamental mode for n suspension units either side of the proof mass is given by

$$k_x = \frac{24EI_x}{nl^3}. \tag{25}$$

There is a considerable price, though, to be paid for reducing the fundamental frequency by this route: the rejection ratio drops precipitously for most of the off-axis modes. Figure 4 shows the rejections ratios as the number of suspension units increases from FEA of a model lateral suspension. The ordering of the rejection ratios for one suspension unit agrees well with the rules of thumb established in the last column of table 1, with the full analytical values of the first column within ±7% of the FEA. As the number of units increases, the FEA rejection ratio drops as approximately $1/n$ for y, z and β; as $1/n^{0.6}$ for γ; as $1/\sqrt{(n)}$ for x_1; and is independent of n for α.

The reduction in the rejection ratios of the y, z and β modes can be explained by considering that the translational compliance of an elastic member increases with the cube of the length of the member, so that while from [25] the fundamental frequency drops inversely as the square root of n, the cross-axis frequencies fall as $1/n^{3/2}$ and so the rejection ratio will scale as $1/n$. The γ mode depends more on the twisting compliance of a member, which increases with the square of the length,

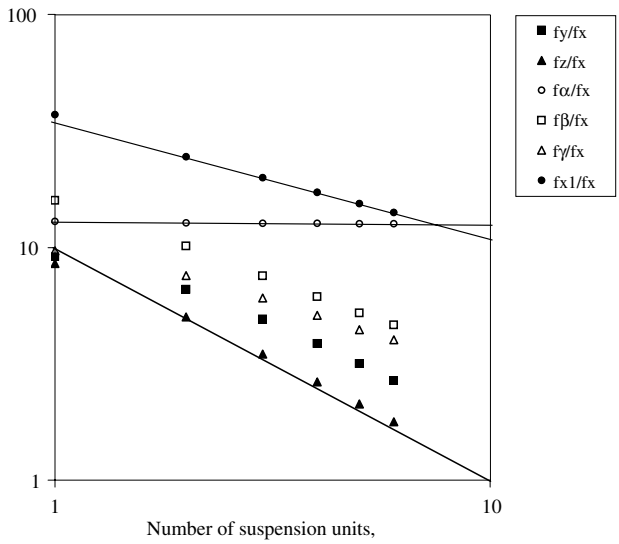

Figure 4. Log–log variation as calculated by FEA of the rejection ratio for the spurious modes as the number of suspension units is increased from 1 to 6. Three fits for the rejection ratio are shown: for x_1, $1/\sqrt{(n)}$; for α, independent of n; for z, $1/n$.

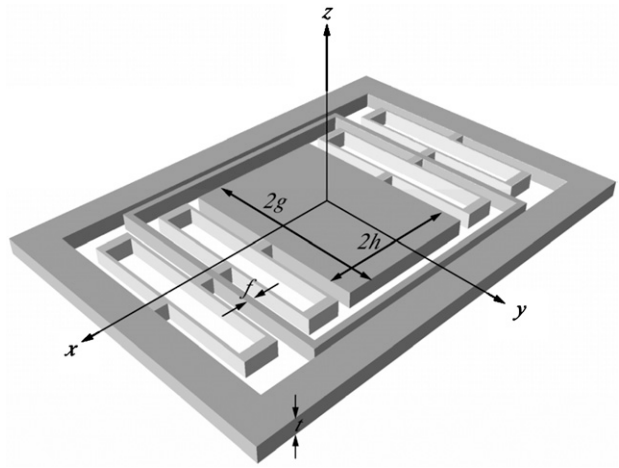

Figure 5. Schematic of a suspension with a intermediate frame between two suspension units.

and hence the rejection ratio might be expected to be inversely proportional to the square root of n, reasonably close to the $1/n^{0.6}$ seen. For the x_1 mode, the mass of the suspension is proportional to n, and so the rejection from (24) will fall as the inverse square root. Like the fundamental, the α mode frequency is inversely proportional to n and so there is no change in the rejection ratio with additional suspension units.

In order to overcome the considerable shortcoming of this drop in the rejection ratios, it is necessary to decouple the additional suspension units, so the off-axis compliances add linearly rather than scale as the cube or square of the units added. Intermediate frames can be introduced into the suspension to increase the cross-axis rigidity. Figure 5 shows a schematic of a suspension with a single intermediate frame. These frames are symmetric about the suspended mass and couple together the two sets of springs on either side of the proof mass. As they join parts of the suspension that move synchronously in the fundamental node, they have very little effect on the fundamental frequency. However, by imposing

Table 2. Expressions for the fundamental and lowest spurious modes for a lateral suspension with multiple (n) suspension units either side of the proof mass and incorporating intermediate frames.

Mode, i	ω_i^2
X	$\frac{24EI_x}{mnl^3}$
Y	$\frac{8EI_x}{mnls^2} = \frac{l^2}{3s^2}\omega_x^2$
Z	$\frac{1/n}{\frac{mls^2}{8GJ}+\frac{mcl^3}{12EI_z}} = \frac{\omega_x^2}{\frac{3EI_xs^2}{GJl^2}+\frac{2cI_x}{I_z}}$
α	$\left\{\frac{4EI_x(s-w)g^2}{GJ_sl^3}+\frac{4I_xg^2}{I_zl^2}\left[1-\frac{3}{4+\frac{3s^2EI_z}{l^2GJ}}\right]\right\}^{-1}\omega_x^2$
β	$3\left[1+(n-1)\frac{(s+f/2)}{h}\right]\omega_x^2$
γ	$\frac{3\left[1+(n-1)\frac{(s+f/2)}{h}\right]}{1+g^2/h^2}\omega_y^2$
x_1	$3\frac{m+nm_{\text{spring}}}{m+n(m_{\text{spring}}+m_{\text{frame}})}\omega_x^2$

additional boundary conditions on the cross-axis modes the frames can greatly increase the frequencies of these modes. The effect of the frames is first analyzed assuming they are massless and perfectly rigid.

Stiffening in the z direction is first considered. The suspension can be subdivided into n sets of one unit each by introducing n-1 frames between each unit. The total deflection will be the sum of the deflections from each set, with the corresponding spring constant from (7) is given by

$$\frac{1}{k_z} = n\left(\frac{ls^2}{8GJ}+\frac{cl^3}{24EI_z}\right). \tag{26}$$

The rejection ratio is therefore unaffected by the introduction of additional spring units. The beneficial effect on the y-axis rejection ratio is identical.

The cross dependence of the rotational rigidities to the translational rigidities produces a corresponding increase in rotational rigidity with the introduction of frames for rotations about the y and z axes. For rotation about the y and z axes, there is a further stiffening as the elastic forces are applied further away from the rotation axis as the number of suspension units increases. The relevant forces for the three-suspension-unit case are shown in figure 6, where the very weak torsional contribution has been neglected as per (28). The overall rotational spring constant will be given by

$$\frac{1}{k_\beta} = \frac{1}{k_zh^2}+\frac{1}{k_z(h+2s+f)^2}+\frac{1}{k_z(h+4s+2f)^2}, \tag{27}$$

where f is the width of the frames. For n spring units this gives, for $s \ll h$,

$$\left(\frac{\omega_\beta}{\omega_x}\right)^2 = 3\left[1+(n-1)\frac{s+f/2}{h}\right] \tag{28}$$

giving a better rejection ratio as n increases. There will be a similar stiffening due to the increased moment arm for in-plane rotations as spring units are added. The corresponding rejection ratio will be given by

$$\left(\frac{\omega_\gamma}{\omega_x}\right)^2 = \frac{3\left[1+(n-1)\frac{s+f/2}{h}\right]}{1+g^2/h^2}. \tag{29}$$

The frames have no effect on rotation about the x-axis as they introduce no additional constraints for this motion. The results for all the modes for n spring units and $(n-1)$ are summarized in table 2.

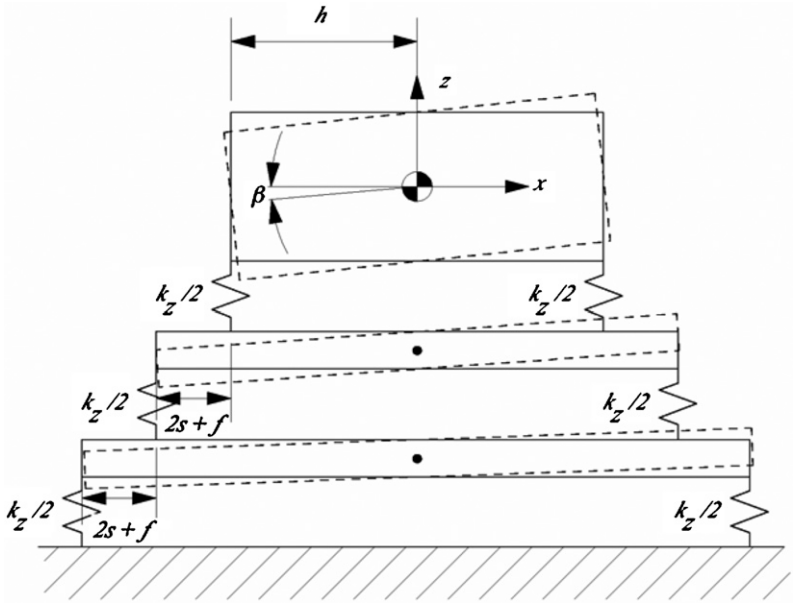

Figure 6. Schematic showing the effective disposition of the spring elements for rotation about the y-axis for three suspension units and two intermediate frames. The torsional spring contributions have been ignored.

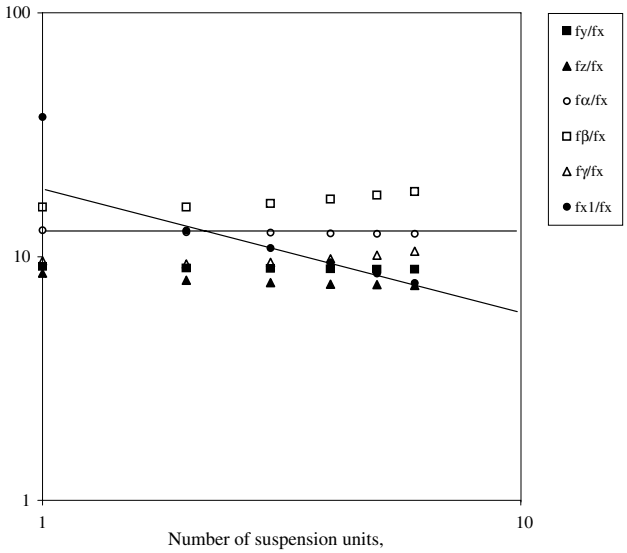

Figure 7. Log–log variation as calculated by FEA of the rejection ratio for the spurious modes of a suspension incorporating intermediate frames as the number of suspension units is increased from 1 to 6. Fits for the rejection ratio are shown: for x_1, $1/\sqrt{(n)}$; for α.

The frames will have a detrimental effect on harmonics along the x-axis due to the increased mass of the suspension. The first harmonic, from (24), will have a frequency of

$$\frac{\omega_{x1}}{\omega_x} = \pi\sqrt{\frac{m}{m_s + m_f}} \tag{30}$$

for a total frame mass of m_f. Therefore the frames should be made as light as possible while maintaining sufficient rigidity. This result is appended to table 2. In figure 7 an FEA calculation of an identical suspension to that modeled in figure 4 is shown. By including intermediate frames into the design, all modes except for x_1 maintain or, in the case of α or γ, slightly improve their rejection ratio as additional suspension units are added, in agreement with the analytical formulae of table 2.

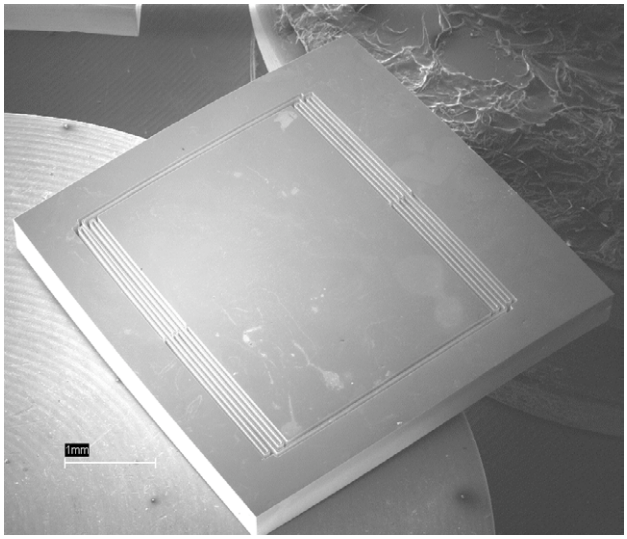

Figure 8. SEM image of a 5 mm die lateral suspension consisting of two spring units and an intermediate frame. The continuous 40 μm wide halo etch used to fabricate the suspension is evident.

3. Experimental details and results

Various suspension geometries have been fabricated (e.g., figure 8) using DRIE to investigate the validity of these dynamic formulae and corrections due to the beam cross-sectional profile. The important parameters for the suspension design analyzed are shown in table 3. Figure 9 shows the details of the suspension corner. The elbows of each suspension unit incorporate lateral webbing to improve the

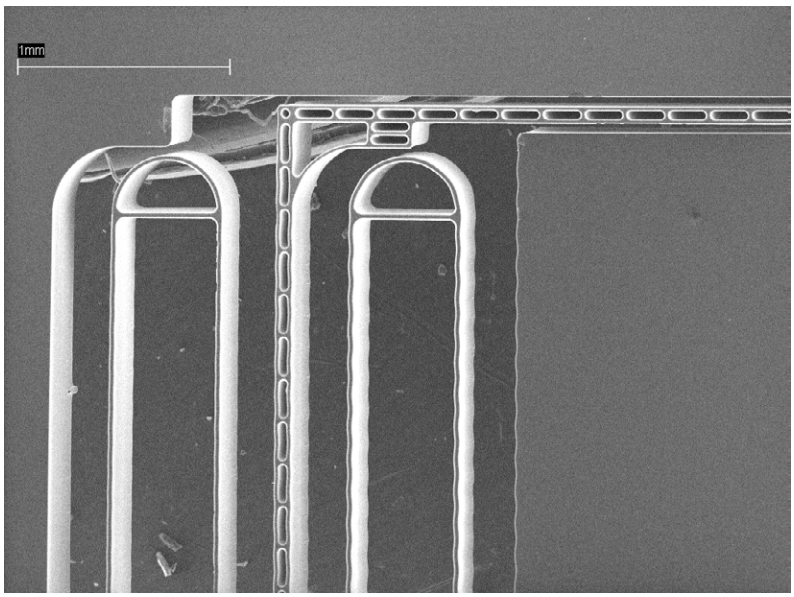

Figure 9. SEM of the corner of a 20 mm die lateral suspension showing the two suspension units and a mass-relieved intermediate frame.

Table 3. Parameters for the three suspension designs tested.

	A	B	C	Source
E (GPa)	122			Si ⟨1 0 0⟩ [33]
G (GPa)	72			Si ⟨1 0 0⟩ [33]
t (μm)	528			SEM profile
w (μm)	24		31	Mask, nominal
I_x (μm^4)	2.64×10^5		5.72×10^5	SEM profile
I_z (μm^4)	2.38×10^8		2.96×10^8	SEM profile
J (μm^4)	1.06×10^6		2.29×10^6	SEM profile
C	1.20		1.20	Mask and FEA as from figure 2
n	1	2	3	
l (mm)	8.32	8.32	8.21	Mask, nominal
s (μm)	627	516	426	Mask, nominal
$g \times h$ (mm)	8.96×6.03	8.84×6.03	8.84×6.03	Mask, nominal
$m/(m_s + m_s)$	42	31	20	Mask and SEM profile from figure 16
w_s (μm)	100	100	140	Mask

rigidity in the z direction. The intermediate frame has been relieved to attempt to minimize the on-axis spurious modes.

DRIE does not produce perfectly rectangular beam cross sections [24–27]. In general DRIE causes some bowing in of the profile causing the beam to be thinner midway through the wafer. As will be seen, this effect of the etch can be appreciable but it can also be readily quantified if the profile is known. Previous work has analyzed this effect for bending of folded cantilevers in the compliant direction if the deviation from the rectangular profile is small [35], but the approximations made are not applicable to the more pronounced etch profiles observed in this work. We have used SEM data from cross sections of the micromachined beams to numerically calculate the second moments of area and the torsional constants of the beams I_x, I_y and J.

The beam profile and sidewall quality are strongly dependent on the etch geometry. Therefore to ensure that the beam profiles remained as uniform as possible across the wafer both within and between different suspension dies, a 'halo' mask was used where etching occurs in a trench of the same width, in this case of 40 μm, across the wafer. The suspensions were etched in nominal 500 μm thick wafers in an STS inductively coupled plasma DRIE. Process parameters are detailed in [27]. Before the etch reached the bottom surface the wafers were mounted on a handle wafer using vacuum-compatible thermally conductive grease (Cool Grease, AI Technology, Princeton Junction NJ, USA). Footing damage was reduced by the prior evaporation of a 500 nm layer of aluminum on the backside of the wafer.

The rigidity of the suspensions was determined using an SEM as a vibrometer [34] and also with an optical microscope to measure the out-of-plane sag. SEM was performed in a LEO VP 1400 (Leica Electron Optics) operated at 30 kV. The dynamic response of the suspension to an external impulse was imaged in the SEM by aligning the fast-scan direction of the beam raster to the compliant x-axis. The suspensions were excited by either an impulse from the stage drive or an external impulse on the microscope column. The scan speed of the raster was then adjusted so that the time period, or several time periods of the dynamics of interest corresponded to the frame

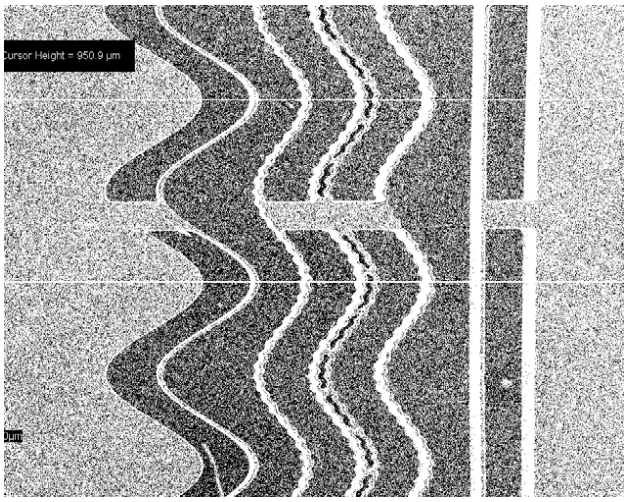

Figure 10. SEM for the determination of the in-plane dynamics for the fundamental and first on-axis spurious mode of the lateral suspension.

acquisition time. For resonant-frequency determinations, frame acquisition times of 50 ms to a few seconds were appropriate. Images were taken at UHV, which for the very high quality factors of the suspensions (up to 40 000 [34]) ensured that a very-nearly-constant-amplitude sinusoid was evident in the image. Figure 9 shows the fundamental mode imaged in the SEM evident as a small-amplitude wave in the edge position of the proof mass. Spurious modes with deflections in the compliant direction can be imaged as superimposed higher frequencies. Figure 10 shows the first on-axis harmonic of frequency ω_{x1} with an antinode at the intermediate frame. One considerable advantage of this technique is that the spurious-mode rejection ratio can be immediately measured as the number of spurious-mode oscillations corresponding to one fundamental oscillation.

By orienting the scan and the suspension with respect to the incident electron beam, modes along multiple axes can be visualized. Several modes can contribute to oscillations in any one SEM image. Identification of the modes and determination of the rejection ratios is most easily performed if only one spurious mode (plus the fundamental if visible) is contributing to the imaged oscillation. Taking first the beam in the z direction with the scan parallel to the compliant direction to visualize oscillations along the x-axis, the total oscillation $X(x, y, t)$ will be a sum of the displacements of all modes, i, that contribute to the overall displacements in the x direction

$$X(x, y, t) = \sum_i X_i(x, y) \cos \omega_i t. \tag{31}$$

In figure 11 the values of $|X(x, y)|$ are shown plotted for the modes with displacement components in the x-direction, namely the fundamental x_0, the on-axis mode due to the finite suspension mass x_1, and the rotation about the z-axis γ. From these the best locations for SEM imaging to separate the modes can be identified (see figure 11(a)), namely at the center of the suspension for the first on-axis spurious mode and at the corner of the proof mass for the rotation about the z-axis. Figure 12 is an SEM to determine ω_γ/ω_x from the two superimposed modes along the edge of the proof mass. Also evident in this

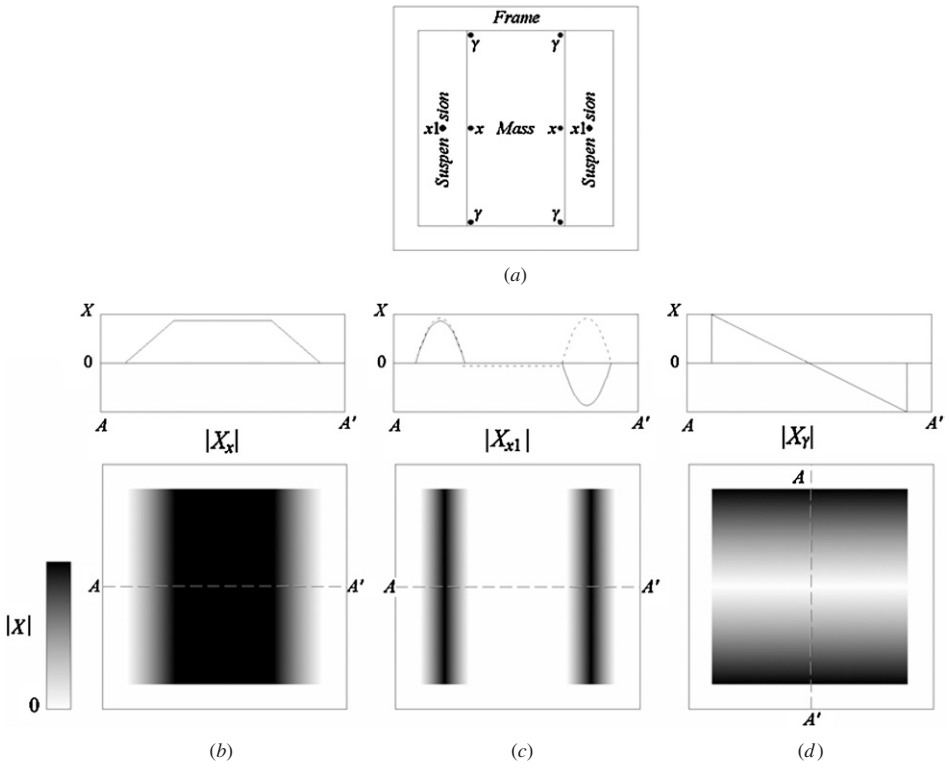

Figure 11. (a) Overall geometry, and amplitude plots $|X_i(x, y)|$ with profiles of the on-axis displacement X_i for (b) the fundamental mode, $i = x$, (c) the on-axis first spurious modes, symmetric ($i = x1_s$, unbroken line in profile plot) and asymmetric ($i = x1_a$, dashed line in profile plot) and (d) the in-plane rotation mode, $i = \gamma$. The locations for best imaging the individual modes are shown in (a).

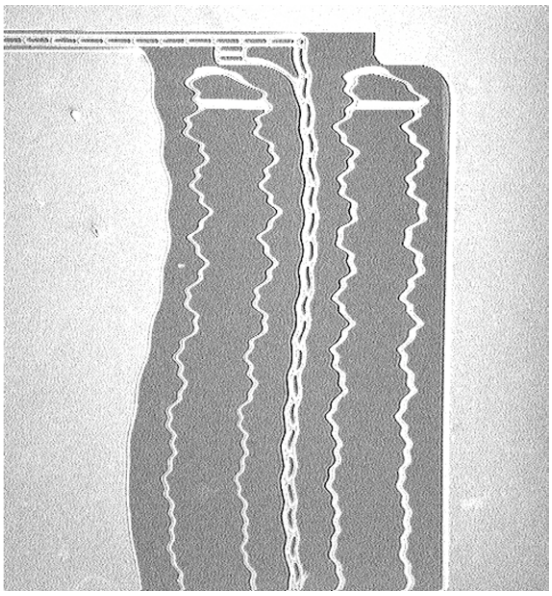

Figure 12. SEM for the determination of the in-plane rotation frequency. Also evident are the superimposed x, x_1 and γ modes toward the suspension elbows.

image is the superposition of all the X modes that occur toward the elbows of the suspension. Rotating the scan by 90° to the y-axis allows visualization of the additional y mode as well as the γ mode (figure 13).

Finally the suspension can also be visualized with the electron beam very nearly along the y-axis (figure 14) if the rigidity in the y-direction is sufficient to prevent interference between the frames. For this viewing angle the displacement can only be visualized in the z direction as a function of x:

$$Z(x,t) = \sum_i Z_i(x)\cos\omega_i t. \tag{32}$$

The z, α and β modes all produce Z displacements (figures 15(c) and (d)) with the first two modes being indistinguishable. The fundamental also produces a visible deflection which allows for direct determination of the rejection ratios. The x-mode deflection is due to the small tilt of the beam direction off the y-axis of one or two degrees providing a component of the proof-mass weight in the z-direction. As the fundamental is excited this component produces a varying z-deflection as the suspensions on each side of the proof mass stiffen and soften, alternately compressing and expanding to produce an effective decrease and increase in s.

Clean excitation of the rotational modes of the suspension is not always achievable, with translational modes sometimes swamping the rotational vibration amplitudes. Therefore a complete determination of all the modes from such a study of the dynamics in the SEM is not always possible.

As well as imaging the modes dynamically in the SEM, it is also possible to determine the frequencies of the three translational modes (x, y and z) from the sag under gravity of the suspension along these axes. Such determinations

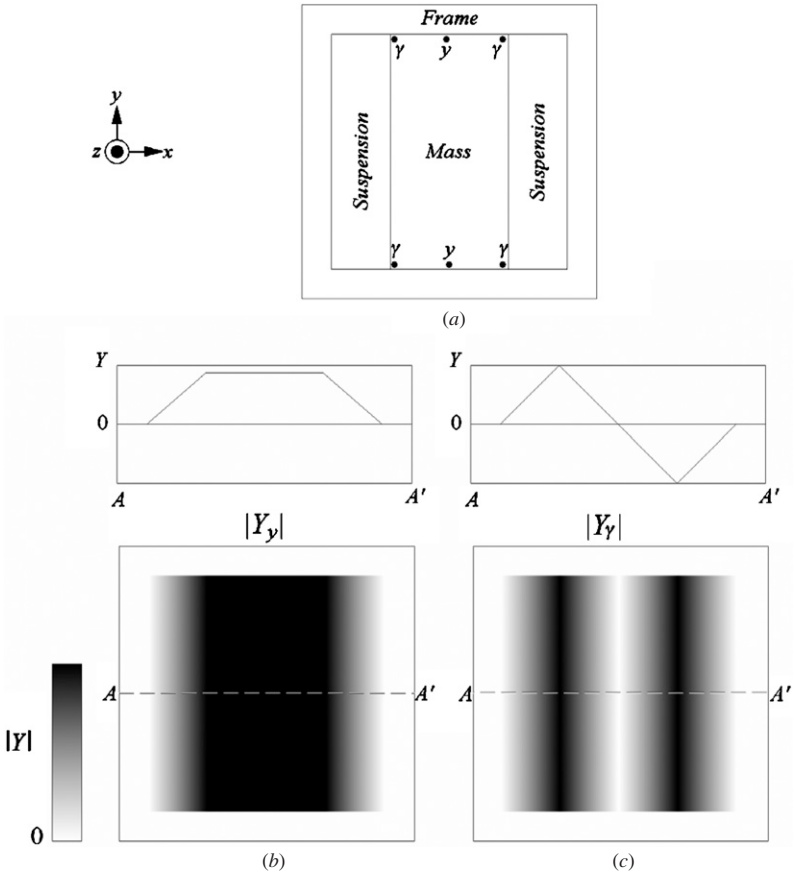

Figure 13. (a) Overall geometry, and amplitude plots $|Y_i(x, y)|$ with profiles of the on-axis displacement Y_i for (b) the in-plane cross-axis mode, $i = y$, and (c) the in-plane rotation mode, $i = \gamma$. The locations for best imaging the individual modes are shown in (a).

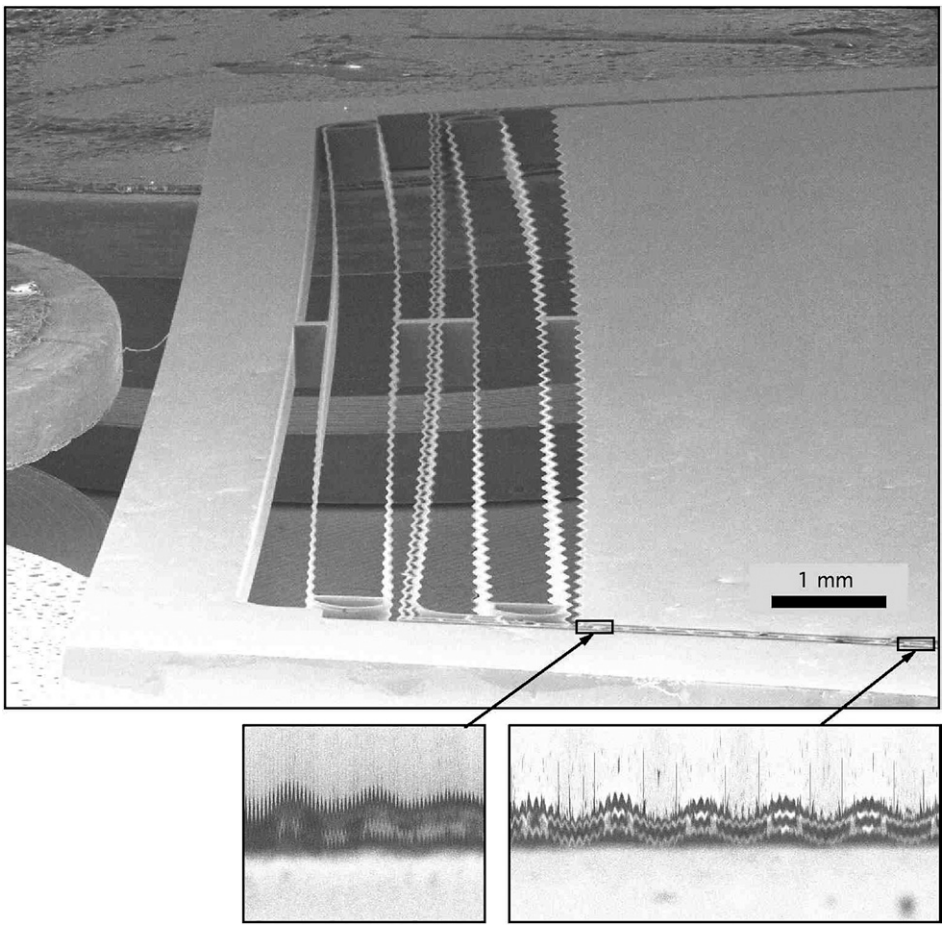

Figure 14. SEMs taken with the suspension tilted with the electron beam close to the y-axis. The main image is taken with the scan direction along the x-axis, while the two insets show the dynamics close to the corner of the proof mass and midway along the proof mass, both with the scan direction along the z-axis.

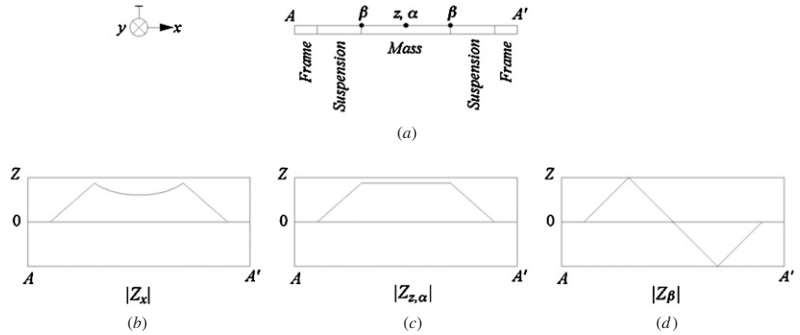

Figure 15. (*a*) Overall geometry and amplitude plots $|Z_i(x)|$ with profiles of the on-axis displacement Z_i for (*b*) the fundamental, $i = x$, and (*c*) the indistinguishable $i = z$ and $i = \alpha$ modes, and (*c*) the $i = \beta$ The locations for best imaging the individual modes are shown in (*a*).

provide an independent check on the dynamically determined frequencies and allow an ambiguous determination of the z mode, which is indistinguishable from the α mode in the dynamic images. In general the sag Δ_i along any axis i will be given by

$$\Delta_i = \frac{g \cos \theta_i}{\omega_i^2}, \tag{33}$$

where g is the gravitational acceleration, θ_i is the angle between the i-axis and the gravitational vector and ω_i is the angular frequency of the translational mode. Applying (33), the x- and y-mode frequencies could be determined from static images in the SEM and the z mode frequency from focus-depth measurements in an optical microscope. The results of these determinations for the three suspensions are shown in table 4.

Figure 16 shows a composite SEM of a cross section of a beam together with a plot of the numerical profile. It is evident that as well as bowing throughout the etch, undercutting is occurring for a few tens of microns below the resist. Using this measured profile, the bending and torsional constants for this beam can be derived.

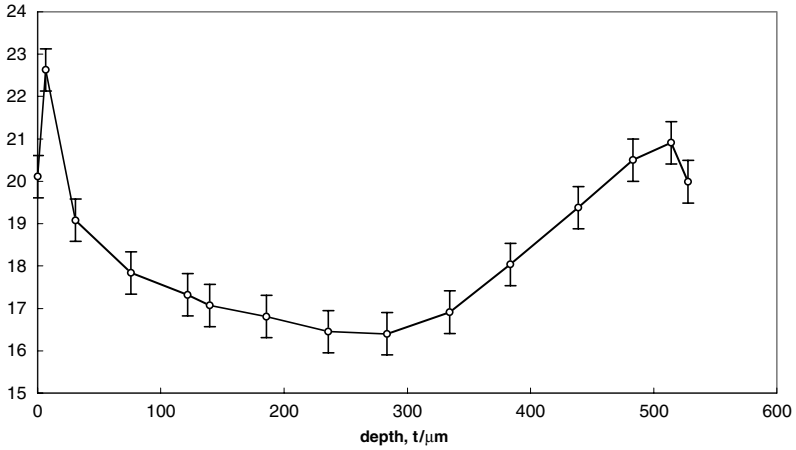

Figure 16. Profile of a suspension beam determined from the cross-sectional SEM.

Table 4. Comparison for the three designs between the spurious-mode values as predicted from the analytical expressions (Form), FEA and observed (Obs).

	A ($n = 1$)			B ($n = 2$)			C ($n = 3$)		
	Form	FEA	Obs	Form	FEA	9.4 ±	Form	FEA	Obs
f_x (Hz)	11.4	11.4	10.7 ± 0.3	8.1	8.1	7.9 ± 0.1	9.9	9.9	10.3 ± 0.2
f_{x1}/f_x	34.5	36	42 ± 2	17.5	14.2	15.7 ± 0.2	14	11.4	12.5 ± 0.5
f_γ/f_x	7.5	8.3	8.5 ± 0.3	9.1	9.5	10.5 ± 0.5	10.9	10.9	11.5 ± 0.3
f_y/f_x	7.7	7.2	6.8 ± 0.4	9.3	8.8	9.4 ± 0.3	11.1	10.5	11.3 ± 0.2
f_z/f_x	10.1	8.3	9.5 ± 0.5	11.5	10.2	11.9 ± 0.2	11.1	11.1	11.5 ± 0.2
f_β/f_x	19.3	15.7	–	23.5	20.5	19.2 ± 0.2	23.5	23.5	–
f_α/f_x	14.9	10.4	–	12.4	13.6	–	14.3	14.3	–

4. Discussion

The etch profile as measured has an appreciable effect on the dynamics of the suspension. Using numerical integration from the measured beam profiles, I_x and J are just 43 ± 4% of their nominal value assuming a rectangular profile with the beam width of the DRIE mask. I_z is less sensitive to the etch profile at 80% of nominal, as the bending constant along the z-axis is mostly determined by the top and bottom parts of the cross section which are least reduced by the overetching. The effect of the etch profile on the bending and torsion constants is incorporated into table 3. From these results an effective beam width, w_{eff}, for the FEA can be derived to give the same $I_x \left(=1/12 t w_{\text{eff}}^3\right)$ and $J \left(=1/3 t w_{\text{eff}}^3\right)$ for a rectangular beam, as both vary as the cube of the width. However, it is not possible in general to simultaneously match I_z, which will vary linearly with the beam width. Hence, we would expect there to be some error in the FEA of the z, α and β modes due to the incorrect value of I_z. For the suspensions studied, however, the total FEA error happens to be rather small, as the cube of the I_z correction factor $(80\%)^3$ is 51% which is reasonably close to the I_x and J correction factor of 43 ± 4%.

The analytical, FEA and observed mode frequencies are generally in very good agreement. Some observed values could not be determined due to the difficulty in cleanly exciting the rotational modes. Inconsistencies in the FEA results due to the incorrect value of I_z are not very evident, as would be expected from the above discussion.

The agreement between analytical, FEA and observed values provides confidence in formulae for the lateral suspensions developed in this work. Further calculations of model suspensions show excellent agreement of FEA and analytical results across a broad range of unfabricated geometries. For example, FEA shows that the best rejection ratio for rotation about the compliant axis is indeed twice the beam aspect ratio, as predicted from [22]. The analytical formulae have the advantage of allowing the immediate characterization of a suspension design and giving a heuristic approach to optimization.

Hence as far as the dynamics of the suspension are concerned, a non-ideal etch profile, if properly incorporated into the design, causes few problems. As the both I_x and J are equally affected by the etch profile, and I_z is increased relative to I_x, a bowed etch profile improves the cross-axis rejection. Furthermore such a profile reduces the mass of the suspension for a given stiffness, improving the rejection of the first on-axis spurious mode. In addition, if conductors are to be routed along the suspension to structures on the suspended mass, a bowed profile has the advantage of a greater surface width being available for a given stiffness of suspension. Hence the optimum beam profile will not in general be rectangular, but will incorporate some overetching, resulting in the beam cross section tending to approach a classical I-beam geometry. Any deviation of mirror symmetry of the beam profile about the center of the wafer can result in cross coupling between modes, a large effect in some suspension geometries [36]. For

the geometry of the lateral suspension of this work the only allowed cross coupling into the compliant direction will be from rotation about the y-axis, and as this coupling takes place due to torsional effects which will be negligible, from (16), for $l \gg s$, the overall effect of any asymmetry in the profile can be neglected.

The introduction of intermediate frames into lateral suspensions has been demonstrated as beneficial to cross-axis rejection in the out-of-plane direction. Intermediate frames should help reject all other modes. The price to be paid for the introduction of the frames is in the lowering of the first compliant-axis harmonic due to the increased mass loading. In this work the mass loading has been minimized by using a relieved structure for the intermediate frames, although at the expense of some loss in torsional strength. There is scope for further optimization of the exact intermediate frame structure. However, at least for the design space of the suspensions in this work, the extra cross-axis stiffness introduced by the intermediate frames outweighs the deterioration of the on-axis dynamics and frames should be incorporated between each suspension unit. In addition to intermediate frames, webbing at the elbows of the suspensions can greatly reduce the out-of-plane bending with little loss of compliance in the on-axis direction. Again, there is scope for optimization of the detailed structure here.

A design heuristic can now be developed and applied for lateral suspensions. The analytical formulae of tables 1 and 2 can be used to first determine the lowest frequency spurious mode of a candidate design. Examination of the parameters will then lead to possible variations on the geometry to push up the rejection ratio of this mode. In general, as the lowest frequency spurious mode is thus pushed away from the fundamental, other spurious modes will be lowered in frequency. For instance, the introduction of frames will improve the rejection of many of the modes but will push down the frequency of the first spurious on-axis mode due to the increase in the suspension mass. The widest separation between the fundamental and first spurious value will therefore occur as the two lowest spurious modes have the same frequency. The three suspensions studied give an example of this approach for an increase in the number of frames (see table 4). As the number of suspension sets increases from one, to two, to three, the lowest rejection ratio is raised while the other spurious-mode rejection ratios decrease. For three suspension sets several modes have a very similar rejection ratio of about (11), representing a near optimum design for a clean bandwidth.

Particular design or performance constraints may cause one mode to be preferentially rejected. An example may be if the out-of-plane z-axis deflection should be minimized to allow for minimum gaps between the suspension and any sandwiching structures. In this case maximizing the rejection of one specific mode may be preferable to overall maximization of the clean, spurious-mode-free, bandwidth above the fundamental.

5. Conclusions

Folded-cantilever structures have been shown to incorporate several desirable features; in particular for the mirror-pair design studied here, the separation of the modes in each degree of freedom. A complete analysis of the important modes of a folded-cantilever suspension has been performed using elastic beam theory, yielding some very simple formulae for all the spurious modes under a relatively non-restrictive set of assumptions. The resulting formulae have been verified for both fabricated suspensions and shown to produce consistent results to FEA over a broader range of model suspensions. A design heuristic for lateral suspensions has been presented. The achieved cross-axis rigidities correspond to an order-of-magnitude frequency ratio between the fundamental and spurious modes of the suspension, corresponding to spring constants two-orders-of-magnitude higher for both the cross-axis translational and rotational modes. Non-ideal etch profiles are shown to have a large effect on the suspension compliance. This effect has been shown to be quantifiable and to ensure that the design goals of the suspension are met it is important that the beam profile is known and predictable. The bowed overetched profile, which most commonly occurs in through-wafer DRIE, has been shown to have a number of beneficial effects on the dynamic performance of the suspension.

In order to improve the rejection of unwanted modes two design features have been demonstrated: the inclusion of webbing at the suspension elbows and intermediate frames coupling portions of the suspension. The latter are particularly effective in increasing the cross-axis rigidities of a lateral suspension and their deleterious effects have been quantified and demonstrated. Although the design has focused on high-aspect-ratio beam geometries, the analytical expressions derived in this work will be applicable to surface-micromachined suspensions.

Acknowledgments

The authors are grateful to Werner Karl, Trevor Semple, Sanjay Vijendran and John Stagg at Imperial for processing of the suspensions, Song Tsai at Imperial for additional FEA, as well as Ian Standley at Kinemetrics Inc. and Richard Syms at Imperial for valuable discussions. Financial support for this work was provided by Kinemetrics Inc., and the UK Particle Physics and Astronomy Research Council under CREST programme grant PP/D006716/1.

References

[1] Tang W C, Nguyen T H and Howe R T 1989 Laterally driven polysilicon resonant microstructures *Sensors Actuators* **20** 25–32

[2] Tang W C, Nguyen T H, Judy M W and Howe R T 1990 Electrostatic-comb drive of lateral polysilicon resonators *Sensors Actuators* A **21** 328–31

[3] Sherman S J, Tsang W K, Core T A, Payne R S, Quinn D E, Chau K H-I, Farash J A and Baum S K 1992 A low cost monolithic accelerometer; product/technology update *Proc. Int. Electron Devices Meeting (San Francisco)* pp 501–4

[4] Analog Devices, Inc. 1995 ADXL05-monolithic accelerometer with signal conditioning *Data Sheet*

[5] van Drieenhuizen B P, Maluf N I, Opris I E and Kovacs G T A 1997 Force-balanced accelerometer with mG resolution, fabricated using silicon fusion bonding and deep reactive ion etching *Proc. Solid State Sensors and Actuators (Chicago)* pp 1229–30

[6] Weigold J W, Najafi K and Pang S W 2001 Design and fabrication of submicrometer, single crystal Si accelerometer *J. Microelectromech. Syst.* **10** 518–24
[7] Ishihara K, Yung C-F, Ayon A A and Schmidt M A 1999 Inertial sensor technology using DRIE and wafer bonding with connecting capability *J. Microelectromech. Syst.* **8** 403–8
[8] Eberhardt W, Gerhauwsser T, Giousouf M, Kuck H, Mohr R and Warkentin D 2002 Innovative concept for the fabrication of micromechanical sensor and actuator devices using selectively metallized polymers *Sensors Actuators* **A 97–98** 473–7
[9] Suzuki Y and Tai Y-C 2003 Micromachined high-aspect-ratio parylene beam and its application to low-frequency seismometer *Proc. Sixteenth Ann. Int. Conf. on Micro Electro Mechanical Systems (Kyoto, Japan)* pp 486–9
[10] Kranz M, Burgett S, Hudson T, Bunickck M, Ruffin P and McKee J 2004 Performance of a silicon-on-insulator MEMS gyroscope with digital force feedback *Proc. Position Location and Guidance Symp. (Monterey, CA)* pp 7–17
[11] Huang W, Syms R R A, Stagg J and Lohmann A 2004 Precision MEMS flexure mount for a Littman tunable external cavity laser *IEE Proc. Sci. Meas. Technol.* **151** 67–75
[12] Grade J D, Jerman H and Kenny T W 2003 Design of large deflection electrostatic actuators *J. Microelectromech. Syst.* **12** 335–43
[13] Peeters E, Vergote S, Puers B and Sansen W 1991 A highly symmetrical capacitive micro-accelerometer with single degree-of-freedom response *Dig. of Tech. Papers Int. Conf. on Solid-State Sensors and Actuators (San Francisco)* pp 97–100
[14] Lemkin M and Baser B E 1996 A micromachined fully differential lateral accelerometer *Proc. Custom Integrated Circuits (San Diego)* pp 315–8
[15] Tamsir A S, Saharil F and Majlis B Y 2002 The optimization of mechanical harmonic modes of the 75 g balanced weight distribution capacitive accelerometer. *Proc. Semiconductor Electronics (Penang, Malaysia)* pp 529–33
[16] Harness T and Syms R R A 2000 Characteristic modes of electrostatic comb-drive *X–Y* microactuators *J. Micromech. Microeng.* **10** 7–14
[17] Weaver W J, Young D H and Timoshenko S P 1990 *Vibration Problems in Engineering* 5th edn (New York: Wiley)
[18] Himelbau H Jr and Rubin S 1996 Vibration of a resiliently supported rigid body *Shock and Vibration Handbook* 4th edn, ed C M Harris (New York: McGraw-Hill) pp 3.1–3.57
[19] Young W C 2002 *Roark's Formulas for Stress and Strain* 7th edn (New York: McGraw-Hill)
[20] Jaecklin V P, Linder C, de Rooij N F and Moret J-M 1993 Comb actuators for *xy*-microstages *Sensors Actuators* A **39** 83–9
[21] Puers B and Lapadatu D 1994 Extremely miniaturized capacitive movement sensors using new suspension systems *Sensors Actuators* A **41** 129–35
[22] Yeh J A, Chen C and Lui Y 2005 Large rotation actuated by in-plane rotary comb-drives with serpentine spring suspension *J. Micromech. Microeng.* **15** 201–6
[23] Zhou G and Dowd P 2003 Tilted folded-beam suspension for extending the stable travel range of comb-drive actuators *J. Micromech. Microeng.* **13** 178–83
[24] Gomez S, Belen R J, Kiehlbauch M and Aydil E S 2004 Etching of high aspect ratio structures in Si using SF_6/O_2 plasma *J. Vac. Sci. Technol.* A **22** 606–15
[25] Laermer F and Urban A 2003 Challenges, developments and applications of silicon deep reactive ion etching *Microelectron. Eng.* **67–68** 349–55
[26] Yeom J, Wu Y and Shannon M A 2003 Critical aspect ratio dependence in deep reactive ion etching of silicon *Dig. of Tech. Papers Int. Conf. on Solid-State Sensors and Actuators (San Francisco)* pp 1631–4
[27] Pike W T, Karl W J, Kumar S, Vijendran S and Semple T 2004 Analysis of sidewall quality in through-wafer deep reactive-ion etching *Microelectron. Eng.* **73–74** 340–5
[28] Analog Devices, Inc. 1998 ±5g to ±50g, low noise, low power, single/dual axis iMEMS accelerometer *Data Sheet*
[29] Luo H, Zhang G, Carley L R and Fedder G K 2002 A post-CMOS micromachined lateral accelerometer *J. Microelectromech. Syst.* **11** 188–95
[30] Park I Y, Lee C W, Jang H S, Oh Y S and Ha B J 1998 Capacitive sensing type surface micromachined silicon accelerometer with a stiffness tuning capability *Proc. Eleventh Ann. Int. Workshop Micro Electro Mechanical Systems (Heidelberg, Germany)* pp 637–42
[31] Gang Z, Huikai X, de Rosset L E and Fedder G K 1999 A lateral capacitive CMOS accelerometer with structural curl compensation *Proc. Twelfth IEEE Int. Conf. on Micro Electro Mechanical Systems* pp 606–11
[32] Suzuki Y and Tai Y-C 2003 Micromachined high-aspect-ratio parylene beam and its application to low-frequency seismometer *Proc. Sixteenth Ann. Int. Conf. on Micro Electro Mechanical Systems*
[33] Kelly A and Groves G W 1970 *Crystallography and Crystal Defects* (Harlow, UK: Longman)
[34] Pike W T and Standley I M 2005 Determination of the dynamics of micromachined lateral suspensions in the scanning electron microscope *J. Micromech. Microeng.* **15** S82–8
[35] Liu R, Paden B and Turner K 2002 MEMS resonators that are robust to process-induced feature width variations *J. Microelectromech. Syst.* **11** 505–11
[36] Laermer F and Urban A 2003 Challenges, developments and applications of silicon deep reactive ion etching *Microelectron. Eng.* **67–68** 349–55